ACS APPLIED MATERIALS & INTERFACES

Research Article

www.acsami.org

Mn-Doped TiO_2 Nanosheet-Based Spheres as Anode Materials for Lithium-Ion Batteries with High Performance at Elevated Temperatures

Wei Zhang,[†] Weidong Zhou,[‡] Jasper H. Wright,[†] Young Nam Kim,[‡] Dawei Liu,*[,†] and Xingcheng Xiao*[,‡]

[†]Kazuo Inamori School of Engineering, the New York State College of Ceramics, Alfred University, Alfred, New York 14802, United States

[‡]Chemical Sciences and Materials Systems Laboratory, General Motors Global R&D Center, Warren, Michigan 48090, United States

Supporting Information

ABSTRACT: Novel Mn^{2+}-doped TiO_2 nanosheet-based spheres have been successfully prepared via a simple hydrothermal and ion-exchange process. After hydrothermal growth, flowerlike nanosheet-based spheres of protonated dititanate were confirmed by scanning electron microscopy (SEM) and transmission electron microscopy (TEM). The hierarchical nanostructure was obtained via a dissolution–recrystallization process starting from a precursor of homogenous TiO_2 nanospheres. Moreover, as-prepared protonated dititanate was converted to Mn-doped nanosheet-based spheres via the ion-exchange method. Then, both the doped and undoped protonated dititanate were calcined and tested as anode materials for lithium-ion battery applications at elevated temperatures. The undoped sample showed an initial capacity of 201 mAh g^{-1} but only had 44.1% of the initial capacity retained after 50 cycles at mixed current densities of 30, 150, and 500 mA g^{-1} at 55 °C, while the Mn-doped one exhibited an initial capacity of 190 mAh g^{-1} and 91.4% capacity retention with superior reversible capacity under the same test conditions. Comparisons between different samples suggest that manganese ions on the surface of TiO_2 nanosheet-based spheres are responsible for the enhanced electrochemical performance.

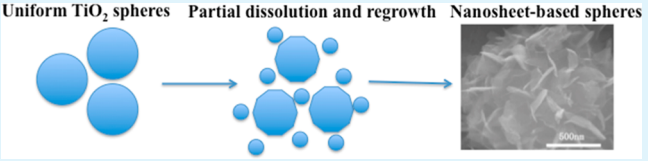

KEYWORDS: *nanosheet-based spheres, protonated dititanate, ion-exchange, lithium-ion batteries*

1. INTRODUCTION

Today, the demand for clean and sustainable energy is becoming more and more critical because of climate change and the decreasing availability of fossil fuels. As powerful energy storage devices, rechargeable lithium-ion batteries (LIBs) have demonstrated their significant roles in mobile applications.[1−5] However, to meet the needs of the soaring market, new generations of LIBs are required with increased power density, wider work-temperature range, improved safety, and lower cost. To achieve this goal, it is very important to improve our understanding of electrochemical phenomena on the electrode/electrolyte interface at the nanoscale, though exploring new functional materials as electrodes of LIBs is also necessary. To date, many studies on this topic have been published by research groups around the world,[6−8] and anode materials will be a key factor in improving the performance of lithium ion batteries due to their impressively higher capacities than cathode materials. However, a large fraction of anode materials suffer poor cyclic stabilities during repeated lithium ion insertion/extraction processes due to the complicated properties of their electrode/electrolyte interface, well known as solid electrolyte interface (SEI). As a result, most anode materials studied in the lab exhibit poor performance in commercial applications. So far, graphite has been used as the anode for most LIBs in practice because of its low electric potential (0.1 V vs Li^+/Li) and high capacity (~300 mA g^{-1}).[9] However, problems include low power density and decomposition of the solid electrolyte interphase (SEI) on lithiated graphite at elevated temperatures, severely limiting its application in future development.[10,11] Therefore, new materials for overcoming these problems need to be developed. Compared to graphite, titanium dioxide (TiO_2) has a relatively higher lithium insertion/extraction voltage (~1.7 V vs Li^+/Li), which can improve the safety of batteries by reducing the excessive formation of SEI and lithium plating on anodes.[12,13] Furthermore, TiO_2 has promising electrochemical properties, high chemical stability, and nontoxicity.[14,15] These characteristics make it a favorable candidate to replace graphite as an anode material for a new generation of LIBs used in some specific applications requiring fast response and high stability in numerous cycles, i.e., start–stop batteries.

However, low intrinsic electrical conductivity (1×10^{-12} scm^{-1}) has impeded TiO_2's application in practice.[16,17] To solve this problem, various TiO_2 nanostructures have been fabricated in order to improve its Li-ion intercalation performance by shortening Li-ion and electron diffusion

Received: January 27, 2014
Accepted: May 8, 2014
Published: May 8, 2014

paths, enlarging the electrode/electrolyte interfacial area, and facilitating strain relaxation during the insertion/extraction processes.[18−21] Among these nanostructures, nanosheets exhibit promising improvement in electrochemical performance because of its larger surface area and excellent structural flexibility.[22] However, its cyclic capacity drops quickly when applied in some specific situations, similar to what has been reported of SnO_2 nanosheets.[23] The reasons are mainly ascribed to the morphology change of TiO_2 nanosheets during cycling, which lead to decreased electroactive area.[24] To solve this problem, one common approach is to modify the surface of electrodes with transition metal ions, transition metals, transition metal oxides and so on. Many methods have been used to accomplish this, such as directly mixing followed by calcination,[25] physical vapor deposition (PVD)[26] and atomic layer deposition (ALD).[27] However, these methods require complicated procedures and induce high cost; in addition, it is still not easy to obtain homogeneously modified nanostructures. Therefore, there is an immediate need for a simple, low cost and reliable synthesis method to fabricate homogeneously modified TiO_2 that can be used as anodes at elevated temperatures.

Herein, we adopt a two-step strategy through synthesis of novel TiO_2 nanosheet-based spheres and doping manganese ions into the structure via an ion-exchange process. This novel nanostructured material exhibits high capacity and cyclic stability when used as a lithium-ion battery electrode at an elevated temperature of 55 °C. Therefore, it is promising as the anode material for a new generation of LIBs.

2. EXPERIMENTAL SECTION

Preparation of Mn-Doped TiO_2 Nanosheet-Based Spheres. Mn-doped TiO_2 nanosheet-based spheres have been synthesized in three steps. First, TiO_2 nanospheres were prepared via a sol−gel process as reported in the literature.[28] In a typical synthesis process, 0.1987 g of hexadecylamine (HDA, 98%, Sigma-Aldrich) was dissolved in 20 mL of anhydrous ethanol (>99.5%, Anhydrous, Sigma-Aldrich), followed by the addition of 0.08 mL of KCl (≥99.0%, Sigma) solution (0.1 M). Then, 0.4525 ml of titanium(IV) isopropoxide (TIP, 97+%, Alfa Aesar) was added under vigorous stirring for 2 mins. The milky white suspension was kept static for 18 h and then centrifuged; the precipitation was washed with ethanol (200 Proof, Ultra-Pure) three times and dried in air at 40 °C. Then, 0.1 g of as-prepared TiO_2 precursor was dissolved in 20 mL of anhydrous ethanol together with 17 mL of ammonium hydroxide (ACS, 30%, Alfa Aesar) and 3 mL of deionized (DI) water. The mixture was then transferred to a Teflon-lined stainless steel autoclave (Parr Instrument Co.), heated to 130 °C and kept static for 72 h. After this treatment, the autoclave was cooled down to room temperature at a rate of 1 °C min^{-1}. The obtained products were washed with DI water three times and the pH was adjusted to 6 by rinsing with diluted HNO_3 (0.1N, Alfa Aesar) solution. Then, the obtained powders were dissolved in 200 mL of manganese nitrate tetrahydrate (98%, Alfa Aesar) solution (0.09 M) under constant stirring for 2 h. After that, it was washed three times by DI water to remove excess Mn ions and dried in air at 40 °C. Finally, the prepared powders were calcined at 400 °C for 3 h. For comparison, TiO_2 powders without Mn-doping were also calcined under the same conditions. Within this study, the samples are designated as TiO_2-PS (precursor sphere), TiO_2-HT (after hydrothermal treatment), HT-400 (after hydrothermal and calcination without Mn ion doping), and HT-Mn-400 (after hydrothermal treatment, Mn ion-exchange process and calcination).

Structural Characterization. The morphology of obtained samples were characterized with scanning electron microscopy (SEM, FEI Quanta 200) and Transmission electron microscopy (TEM, JEM-2100F) with the accelerating voltage at 20 kV and 200 kV, respectively. The phase structures were determined by X-ray diffraction (XRD, Bruker D2) on a Scintag diffractometer with Cu$K\alpha_1$ radiation (λ = 1.54060 Å) at a scanning rate of 0.017°s^{-1} in the 2θ range from 5 to 75°. The surface element composition was measured by energy dispersive spectroscopy (EDS) using the FEI Quanta 200 and X-ray photoelectron spectroscopy (XPS, VG Multilab 2000, Thermo Electron Corporation) with A1Kα X-ray as the excitation source. The nitrogen adsorption and desorption isotherms were collected at 77 K in the range of relative pressures of 0.0002-0.99P/P_0 using a TriStar II 3020 surface area and porosity measurement system (Micromeritics Instrument Corp.) and used for measurements of the pore size distribution in the 1.7−300 nm range. After drying the powder under a vacuum at 80 °C for at least 12 h, 50−100 mg of each powder sample was degassed under a N_2 gas flow at 150 °C for at least 1 h before weighting and gas sorption measurements. The pore size distribution was calculated using the Barrett−Joyner−Halenda (BJH) methods, using Micromeritics DataMaster software.

Electrochemical Evaluation. Electrochemical impedance spectroscopy (EIS) study was carried out using a Bio-Logic VMP3 Potentiostat analyzer. The frequency range was from 100 kHz to 0.1 Hz. Lithium ion battery performance tests were carried out with a half-cell configuration using CR-2032 coin cells. Li foil was used as both the counter and reference electrode. The working electrode was prepared by mixing active materials (85%), black carbon (Alfa Aesar, 10%), and polyvinylidene fluoride (PVDF, Alfa Aesar, 5%) in *N*-methyl-2-pyrrolidone (NMP, Alfa Aesar). After uniform stirring, the above slurries were coated on copper foil and dried at 120 °C in vacuum for 6 h. Then, the electrode was pressed and cut into disks before assembly in an Argon-filled glove box for coin-cell assembling. 1 M $LiPF_6$ in a mixed solution of ethylene carbonate and diethyl carbonate (1:2 volume ratio, Novolyte, USA) were used as the electrolyte. Galvanostatical discharge/charge tests were performed using an Arbin-BT 2000 measurement system in the potential window of 1-2.5 V versus Li^+/Li at different current densities of 30, 150, and 500 mA g^{-1} at both room temperature and 55 °C.

3. RESULTS AND DISCUSSION

3.1. Characterization of Mn-Doped TiO_2 Nanosheet-Based Spheres. TiO_2 nanosheet-based spheres were prepared as explained in the Experimental Section. As shown in Figure 1a, the uniformity of monodisperse spheres were investigated by SEM. The size of a single particle is around 600-700 nm. Images b and c in Figure 1 show the low- and high-magnification SEM images of hydrothermally prepared nanosheet-based spheres (TiO_2-HT). Compared to the sphere precursor, their morphology changes dramatically. It can be observed that the spheres turn into flower-like structures formed by nanoflakes. Figures 1d and e show the SEM images of samples after calcination at 400 °C for 3 h without and with Mn ion doping (HT-400 and HT-Mn-400). As shown in these two images, little morphology difference can be found between them and they are also similar to TiO_2-HT (Figure 1b). Figure 1f shows the TEM image of HT-Mn-400. It can be found that HT-Mn-400 possesses a solid sphere core. Although SEM and TEM images do not show noticeable morphology change among these three samples, nitrogen adsorption isotherms and XRD patterns reveal obvious differences between them in surface area and crystallinity (to be discussed later).

To investigate the doping effect of the ion-exchange process, surface element compositions of HT-400 and HT-Mn-400 were studied by EDS and XPS. As shown in Figure 2, HT-400 has no manganese element peak existing in the spectrum (Figure 2a), whereas HT-Mn-400 has visible manganese element peaks (Figure 2b). Furthermore, the molar ratio of Mn ions in HT-Mn-400 is 3.1%, which is much higher than the EDS test result

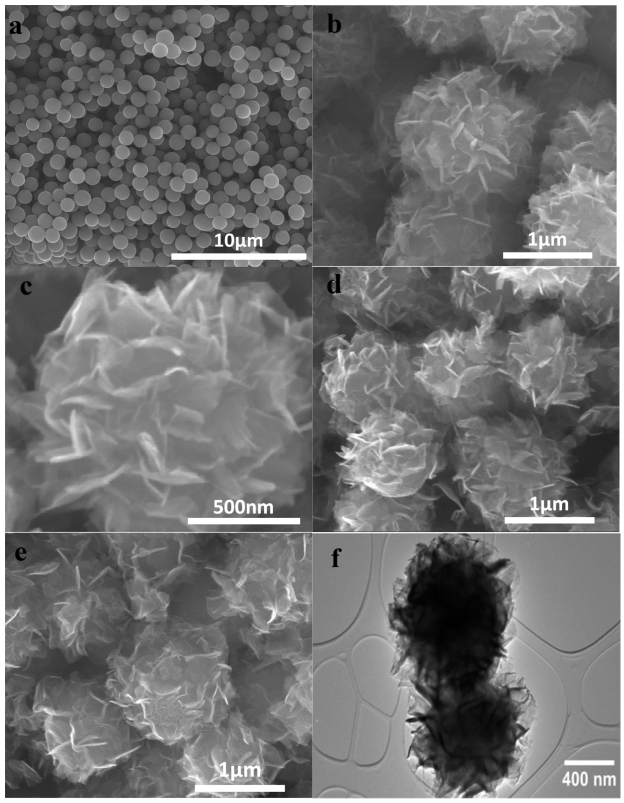

Figure 1. SEM and TEM images of TiO_2 nanostructures obtained after different processes: (a) TiO_2 nanospheres (TiO_2-PS), (b, c) low- and high-mignification SEM images of TiO_2 nanosheet-based spheres synthesized via hydrothermal process (TiO_2-HT), (d) TiO_2 nanosheet-based spheres calcined at 400 °C for 3 h (HT-400), (e, f) SEM and TEM images of TiO_2 nanosheet-based spheres doped by manganese ions, and then calcined at 400 °C for 3 h (HT-Mn-400).

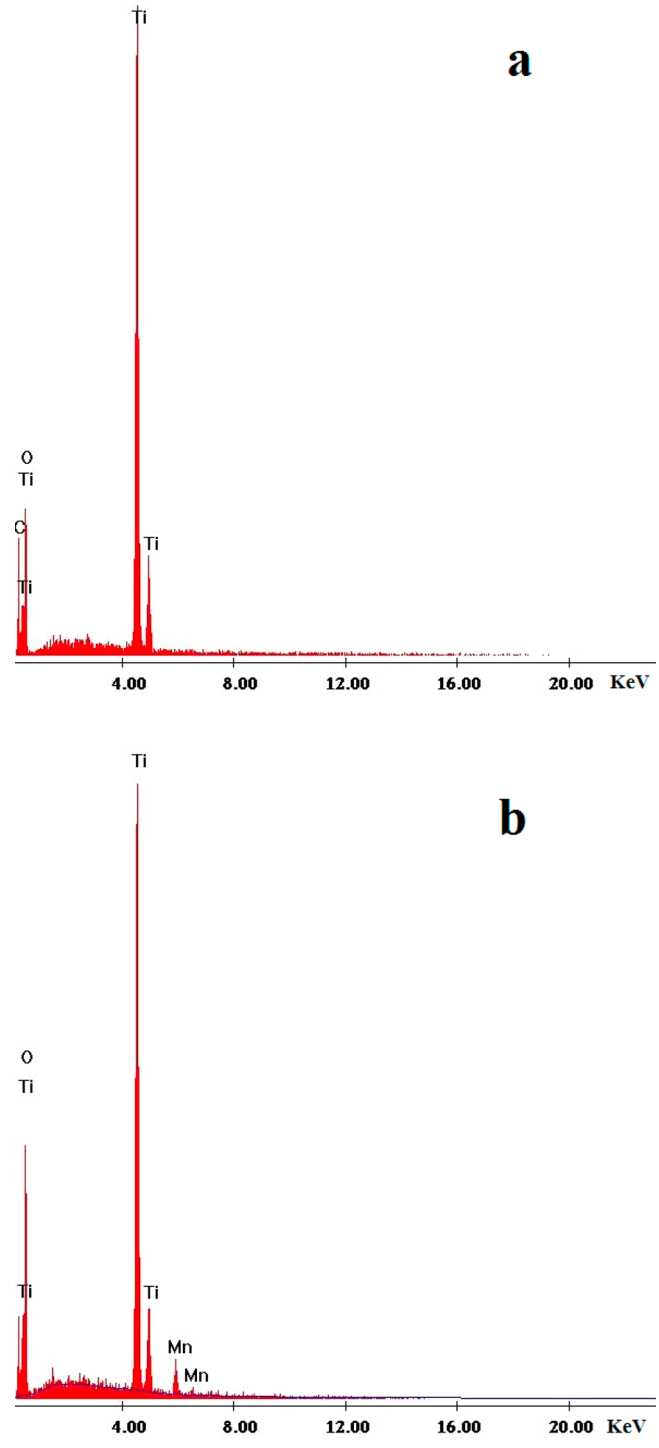

Figure 2. EDS spectra of TiO_2 samples treated (a) before and (b) after Mn ion-exchange process.

of 1.9% of TiO_2 nanotubes reported by Szirmai et al. using a similar ion-exchange process.[29]

Figure 3 shows the XPS spectra of HT-400 and HT-Mn-400. Mn 2p peaks are clearly identified in the spectrum of HT-Mn-400, while there is no corresponding peaks existing in the spectrum of HT-400 (Figure 3a). It agrees well with the EDS result, which indicates that ion-exchange processing an effective method to dope Mn ions in the TiO_2 nanostructure. High resolution XPS spectrum in Figure 3b shows that Mn 2p peaks are with binding energies of 641.4 eV for $2p_{2/3}$ and 653.9 eV for $2p_{1/2}$, which indicates that the oxidation state of Mn ions is 2+. And it can be further confirmed through the unique satellite feature around 647 eV, which is not shared by the other oxidation states of Mn ions.[30−32] This result indicates that the Mn ions oxidation state will not change after calcination at 400 °C for 3 h.

To get more insights into the influence of the doping and calcination processes on TiO_2 samples, nitrogen adsorption-desorption measurments were conducted to characterize the specific surface areas of TiO_2-PS, TiO_2-HT, HT-400, and HT-Mn-400. Figure 4 shows their adsorption and desorption isotherm curves. The isotherm curves of TiO_2-HT, HT-400, and HT-Mn-400 exhibit the typical adsorption hysteresis that belongs to type IV isotherm curves, indicating that these three samples have mesoporous structures.[33] Their specific surface areas are calculated using the BJH method to be 110.7, 230.7, and 222.0 $m^2\ g^{-1}$, respectively. All of these samples have higher specific surface areas than TiO_2-PS (4.5 $m^2\ g^{-1}$), which has type II isotherm curve with little porosity. Furthermore, it also can be found that TiO_2-HT and HT-Mn-400 possess nearly the same specific surface area, whereas HT-400 possesses only about half as much. It is well-known that a decrease in surface area is a common phenomenon after calcination because of particle agglomeration.[34] However, the surface area of Mn-doped TiO_2 does not show any decrease after calcination compared to TiO_2-HT, which did not receive any heat

dx.doi.org/10.1021/am500604p | ACS Appl. Mater. Interfaces 2014, 6, 7292−7300

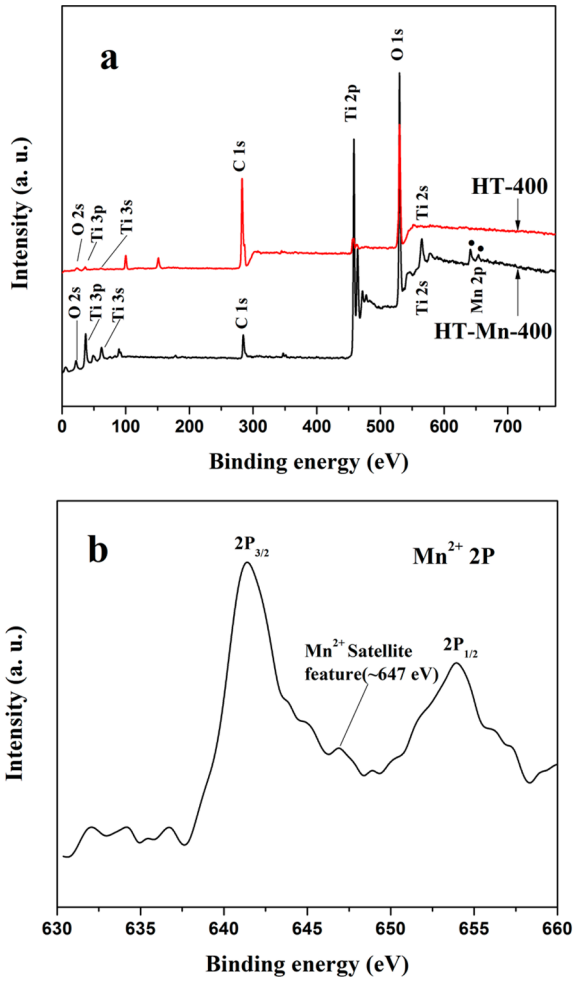

Figure 3. XPS spectra of TiO_2 samples: (a) wide-scan spectra of HT-400 and HT-Mn-400, (b) high-resolution XPS Mn 2p peaks of HT-Mn-400.

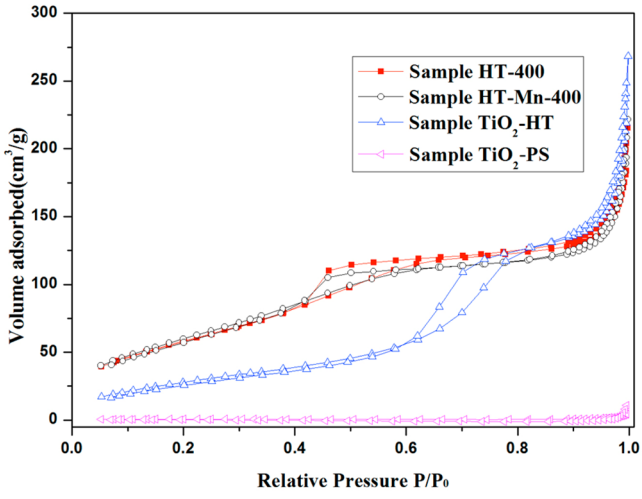

Figure 4. Nitrogen sorption isotherms of TiO_2-PS, TiO_2-HT, HT-400, and HT-Mn-400.

treatment. When the calcination temperature was raised to 500 °C, the morphology of Mn ions doped sample exhibits noticeable change. Nanosheets of the spheres become thicker and start to agglomerate with each other (Figure S1). Above results indicate that Mn ions doping will enhance the structure stability of the TiO_2 nanosheet-based spheres when the calcination temperature is lower than 500 °C.

Figure 5 shows the XRD patterns of TiO_2-HT, HT-400, and HT-Mn-400. As can be found, TiO_2-HT shows a diffraction

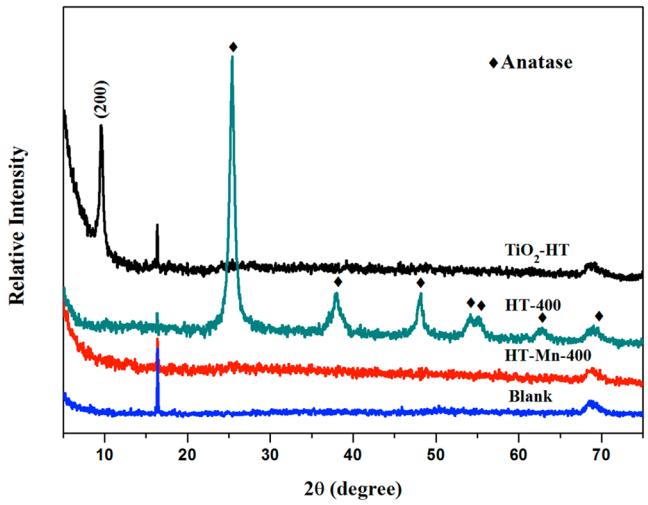

Figure 5. XRD patterns of and TiO_2-HT, HT-400, HT-Mn-400 and the blank sample holder, the diffraction peaks of $2\theta \approx 16$ and 74° existing in all four samples are the background peaks of substrate.

peak of $2\theta \approx 9.7°$, which is assigned to the hydrogen peak of protonated dititanate (PDF, 047-0124). When calcined at 400 °C for 3 h, without Mn ion doping, TiO_2 nanosheet-based spheres (HT-400) show a typical anatase crystal structure. However, when Mn ions are doped via ion-exchange before heat treatment (HT-Mn-400), there is almost negligible intensity of anatse peaks in the XRD pattern. Even when the calcination temperature is increased to 500 °C, the atanase peak of Mn ions doped TiO_2 is still not well-defined (see Figure S2 in the Supporting Information). In addition, there is no manganese compounds peaks existing in the XRD pattern of HT-Mn-400, which suggests that Mn ions have been inserted into the lattic of TiO_2. As demonstrated by relevant studies, impurity ions could act as a strong barrier to the phase transition during calcination. Similar inhibition effects on the TiO_2 phase transition have been reported by other groups doping with various ions and methods.[35,36] On the basis of the BET and XRD tests, we can conclude that Mn ions doping process improved the structure stability and inhibited the crystallization of the TiO_2 nanosheet-based structure.

3.2. Growth Mechanism of Mn-Doped TiO_2 Nanosheet-Based Spheres. On the basis of the above results, we believe that the formation of these nanosheet-based spheres via hydrothermal processing is a modified dissolution-recrystallization process as reported in the literature.[37−40] The growth process is depicted schematically in Figure 6. First, in a hot and alkaline condition, the precursors of TiO_2 nanospheres were partially dissolved in the mother solution to form a small quantity of $Ti(OH)_4$ and a large quantity of free titanate ions after complex chemical reactions. As the process continues and the mother solution becames supersaturated, the dissolved ions will initiate anisotropic regrowth on the surface of the reacted TiO_2 spheres to form flowerlike sphere structures, which is driven by thermodynamic force to reduce the structure's total surface energy.[41] As the mass diffusion and ripening process proceeded, nanosheets continued to grow until small nano-

dx.doi.org/10.1021/am500604p | ACS Appl. Mater. Interfaces 2014, 6, 7292−7300

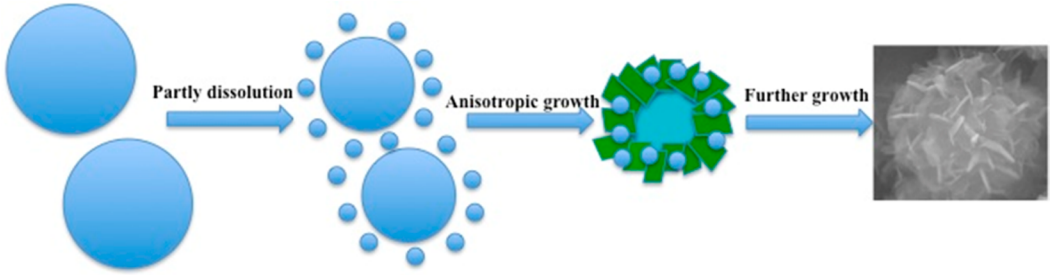

Figure 6. Growth schematic of TiO_2 nanosheet-based spheres prepared by a hydrothermal process.

particles were totally consumed; thereby the uniform nanosheet-based spheres were fabricated via a dissolution−recrystallization process.

Furthermore, it can also be deduced that the obtained TiO_2 nanosheets have been converted to ammonium titanate $[(NH_4)_2Ti_2O_5{\cdot}H_2O]$ at least on the surface of the structure during this hydrothermal process according to findings of similar experiments in the literature.[38,41−44] NH_4^+ was later replaced by H^+ in acid solutions during the washing process and $[(NH_4)_2Ti_2O_5{\cdot}H_2O]$ was converted to protonated dititanate $(H_2Ti_2O_5{\cdot}H_2O)$. The existence of $H_2Ti_2O_5{\cdot}H_2O$ was confirmed by the XRD diffraction pattern of TiO_2-HT. As shown in Figure 5, after hydrothermal and acid washing treatment, the nanosheet structure of TiO_2-HT exhibits a strong peak at $2\theta \approx 9.7°$ corresponding to the (200) lattice plane that fits the PDF card of $H_2Ti_2O_5{\cdot}H_2O$ (047-0124)'s first strongest diffraction peak. It indicates that protonated dititanate exists in HT-400. Then, protons in as-prepared $[H_2Ti_2O_5{\cdot}H_2O]$ were exchanged by manganese ions (Mn^{2+}) to obtain Mn^{2+} doped $Mn_xH_{4-x}Ti_2O_6$.

Compared to NaOH solution, which is usually used in the hydrothermal process to obtain $Na_2Ti_3O_7$,[29,41−44] NH_4^+ can be easily exchanged by H^+ in acidic solutions because of the larger hydrated ionic radius than Na^+,[45] which can increase the amount of obtained $[H_2Ti_2O_5{\cdot}H_2O]$ for the following Mn^{2+} ion-exchange treatment. Although protonated dititanate has been frequently synthesized via hydrothermal growth together with acid solution ion exchange,[38,39,41−43] there are few reports about further ion-exchange of prepared $H_2Ti_2O_5{\cdot}H_2O$.[46] Here, we report on further ion-exchange synthesis of Mn-doped TiO_2 nanosheet-based spheres using $H_2Ti_2O_5{\cdot}H_2O$ as the precursor.

3.3. Lithium-Ion Intercalation Properties Investigation. To study the effects of Mn doping on improving the performance of TiO_2 nanosheet-based spheres as lithium-ion storage electrodes at elevated temperatures, we investigated lithium-ion insertion/extraction properties of HT-Mn-400 by galvanostatic discharge/charge measurements at both room temperature and 55 °C for 50 cycles. To make comparisons, HT-400 and TiO_2-HT were also tested under identical conditions. Measurements at rooms temperatures indicated that all the tested samples possessed similar initial capacities but HT-Mn-400 exhibited better cyclic stability (see Figure S3 in the Supporting Information). It is well-known that when the testing temperature of lithium ion batteries is increased to more than 50 °C, the capacity of batteries increases at the cost of cyclic stability. So in our study, we are focusing on studying the battery performance at 55 °C. Figure 7 shows the discharge and charge curves of these three samples in the first and last 3 cycles at a discharge/charge current density of 30 mA g^{-1} at the testing temperature of 55 °C. It is observed that the initial discharge capacities of HT-400, HT-Mn-400 and TiO_2-HT are 201, 190, and 240 mAh g^{-1}, respectively. As shown in Figure 7a, HT-400 shows noticeable plateaus at approximately 1.8 V (discharge process) and 1.9 V (charge process) during the first 3 cycles, which is similar to reported nanostructured anatase.[17,47] During the first discharge process, TiO_2 voltage drops rapidly from the open circuit voltage (OCV) to 1.8 V and reaches a plateau, which suggests that phase transition from a Li-poor phase to a Li-rich phase occurs. After that, it gradually decreases to the cut-off voltage of 1.0 V. In the last 3 cycles, the discharge plateaus decline to a lower voltage at approximately 1.5 V and become much less well-defined, while the charge plateaus disappear. Correspondingly, the discharge capacity is only 89 mAh g^{-1} at the 50th cycle. However, this decline is not seen in HT-Mn-400. In contrast to HT-400, the initial discharge curve of HT-Mn-400 exhibits a sloping manner from a much lower OCV as shown in Figure 7b, suggesting less pure TiO_2 phase because of Mn-ion doping. In the 2nd cycle, the discharge curve exhibits a much smaller plateau with similar position to that of HT-400. This phenomenon resembles what was reported of V_2O_5 xerogel films with oxygen vacancies on the surface[48] and reveals a more complicated interface formation on HT-Mn-400, which can be ascribed to doped ions on the surface of the nanostructures. In addition, the position and size of these plateaus exhibit little change after cycling. Compared to HT-400 and HT-Mn-400, TiO_2-HT shows a sloping profile of voltage−capacity relationship during the discharge and charge processes (Figure 7c). These curves are typical for electrode materials with amorphous structure due to the absence of heat treatment. In addition, its capacity exhibits noticeable degradation in the initial cycles. XRD patterns of the HT-400 electrode and the HT-Mn-400 electrode after cycling were also studied and compared with those before cycling in Figure S4 in the Supporting Information. The HT-400 electrode shows a significant decay on crystallinity. The fine anatase crystal peaks almost disappear after the cycling (see Figure S4a in the Supporting Information), while the XRD patterns of the HT-Mn-400 electrode show little peak intensity change before and after cycling.

Above results indicate that anatase structure deteriorates severely during cycling at the elevated temperature for HT-400, while HT-Mn-400 exhibits little structure change in the same process.

Figure 8 displays the cyclic performance of HT-400, HT-Mn-400, and TiO_2-HT at different current densities of 30, 150, and 500 mA g^{-1} in the potential window of 1−2.5 V at the testing temperature of 55 °C. As shown in Figure 8a, the discharge capacity of HT-400 increases from 201 mAh g^{-1} to 224 mAh g^{-1} after the first 5 cycles at the discharge current density of 30 mAg^{-1}. However, it drops very quickly in the subsequent 5 cycles to 167 $mAhg^{-1}$ at the same discharge current density.

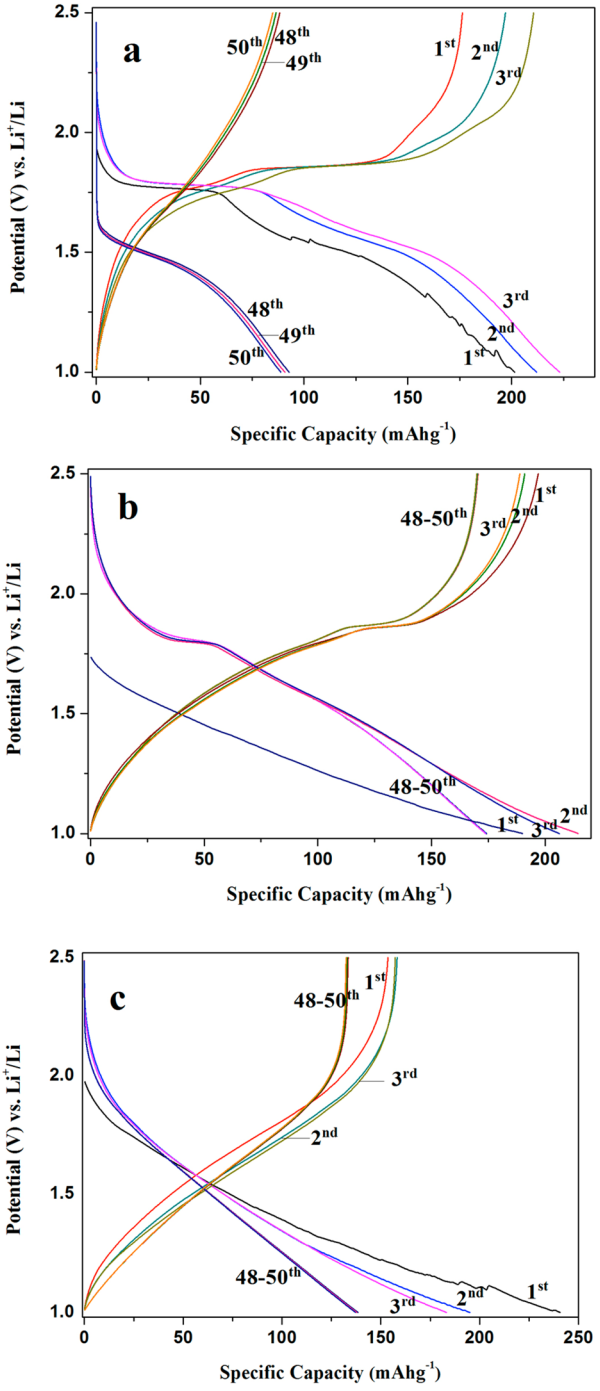

Figure 7. Galvanostatic discharge (lithium insertion)/charge (lithium extraction) curves vs. Li^+/Li of (a) HT-400, (b) HT-Mn-400, and (c) TiO_2-HT cycled at a current density of 30 mA g^{-1} in the first 3 and last 3 cycles of the 50-cycle tests.

When the discharge current density is increased to 150 mA g^{-1} at the 11th cycle, the capacity drops to 125 mAh mg^{-1} when the discharge current density is further increased to 500 mAg^{-1} at the 21st cycle, the discharge capacity drops to 44 mAh g^{-1}. After the discharge current density is changed back to 30 mAg^{-1} at the 41st cycle, the discharge capacity recovers to 69 $mAhg^{-1}$ and increases to 89 $mAhg^{-1}$ at the 50th cycle, with a capacity retention ratio of 44.1 % after 50 cycles at different current densities. In contrast, HT-Mn-400 starts with a little lower initial discharge capacity of 190 mAh g^{-1} but experiences much less capacity degradation in the first 10 cycles. The rate capability of HT-Mn-400 is also obviously better than HT-400: its discharge capacity is 169 mAh g^{-1} at a current density of 150 mAh g^{-1} and 147 mAh g^{-1}at a current density of 500 mAh g^{-1}. When the current density is changed back to 30 mAh g^{-1}, its discharge capacity is 173 mAh g^{-1} which shows little capacity fading in the following cycles and is still as high as 174 mAh g^{-1} at the 50th cycle. The capacity retention rate is 91.4 % after 50 cycles at different current densities (Figure 8b). In addition, the coulombic efficiency of HT-Mn-400 is above 97% during the whole testing process except in the initial cycles, indicating that this sample has a superior reversible capacity that contributes to the good cycling stability. For comparison, we also tested the capacity performance of TiO_2 nanosheet-based spheres without any doping or calcination (TiO_2-HT). In Figure 8c, its capacity drops from 240 to 153 mAh g^{-1} after the first 10 cycles at the low current density of 30 mA g^{-1}, and the coulombic efficiency is lower than 95%. As the test continues, the capacity has a little fading at different current densities; after 50 cycles, the capacity is 137 mAh g^{-1} and the capacity retention is 57.0%.

All of these electrochemical results indicate that Mn-doped TiO_2 samples have noticeably better Li-ion storage capability than undoped ones when used as an anode at an elevated temperature of 55 °C. Furthermore, the kinetic properties of these samples are also measured by electrochemical impedance spectroscopy (EIS). As shown in Figure 8d, the equivalent circuit (Figure 8d inset), R_s and R_{ct} are the ohmic resistance (total resistance of the electrolyte, separator and electrical contacts) and charge transfer resistance, respectively, and W represents the Warburg impedance of Li ion diffusion into the active materials. CPE is the constant phase-angle element, involving double layer capacitance. The system resistance of Rs is similar for HT-400, HT-Mn-400, and TiO_2-HT because of the fact that both materials are grown directly on the substrates that are used at the current collectors, which ensures good electrical conductivity in the electrodes. The charge transfer resistance R_{ct} after cycling for the three samples is in the order of HT-400 (270.6 Ω) > TiO_2-HT (39.7 Ω) > HT-Mn-400 (18.6 Ω), which indicates that Mn-ion doping can improve the charge transfer process at the electrode/electrolyte interface and maintain good electronic conductivity during long-term cycling. Thus, these improved interface properties are considered to be a factor in improving the performance of Mn-doped TiO_2. Together with the results from XRD and BET tests (Figures 5 and 4), we can deduce the effects of Mn-ion doping in this experiment as follows: during ion-exchange, Mn^{2+} replaced some of the H^+ in the structure of $H_4Ti_2O_6$ to form a multi-structure, which improved the structure stability of flower-like TiO_2 nanosheets,[49] i.e., it inhibited the crystal structure conversion under thermal treatment. As a result, the specific surface area and crystal structure of Mn-doped sample HT-Mn-400 had little change after calcination compared to the uncalcined sample TiO_2-HT. Meanwhile, doped Mn ions modified the surface chemistry of TiO_2 nanosheets and maintained their good interface electronic conductivity during long-term cycling. It took a couple of cycles for HT-Mn-400 to build up a more stable interface between the electrode and electrolyte in the electrochemical test. This could explain very well why the discharge curve shape of HT-Mn-400 did not stabilize until the 3rd discharge/charge cycle. This stable interface contributed to the surface integrity of the Mn-doped TiO_2 electrode at elevated temperatures, as evidenced by the cyclic stability improvement during lithium ion insertion/

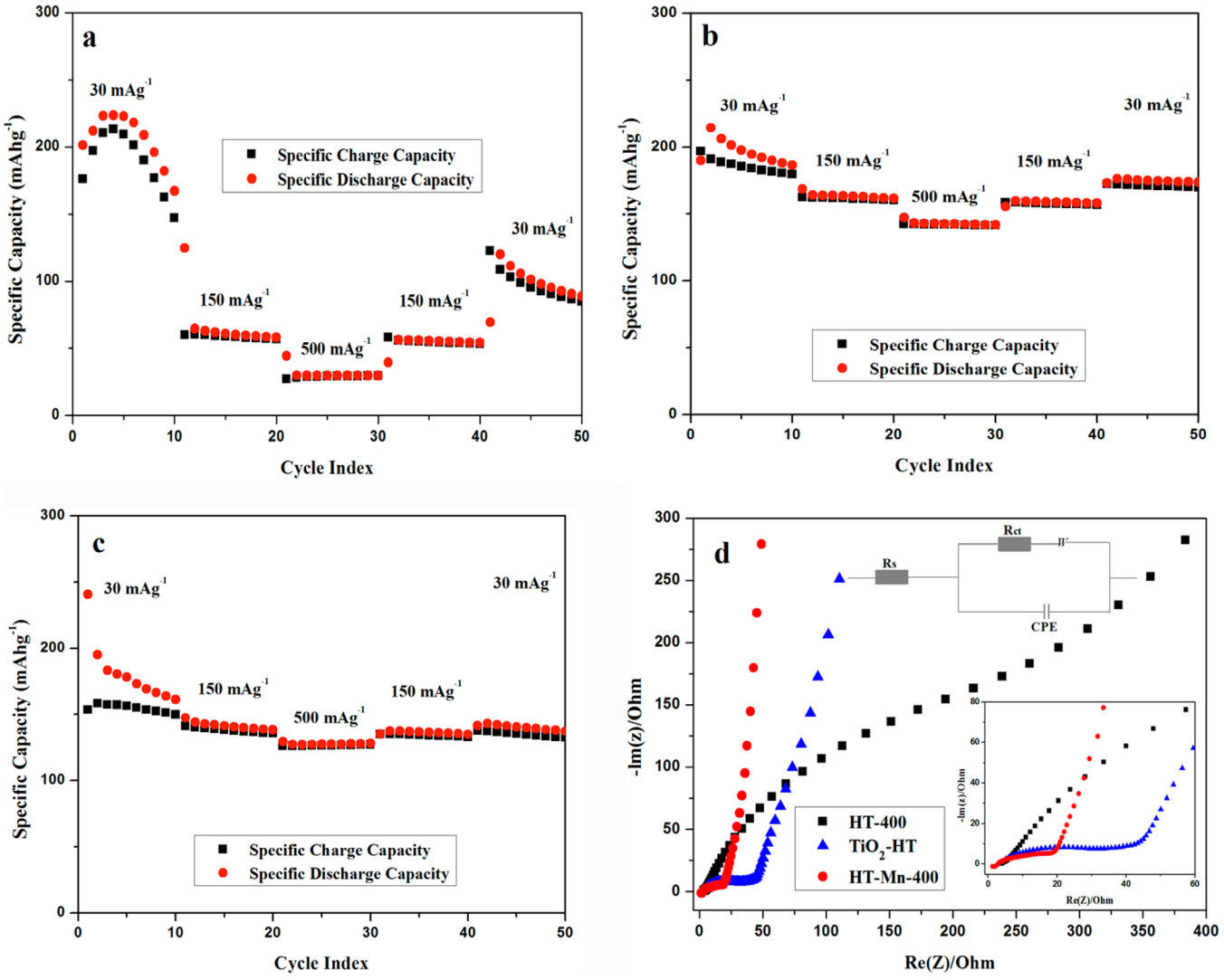

Figure 8. Charge/discharge capacity vs. cycle number of (a) HT-400, (b) HT-Mn-400, and (c) TiO_2-HT cycled at different current densities of 30, 150, and 500 mA g^{-1}. (d) Nyquist plots of HT-400, HT-Mn-400, and TiO_2-HT after cycling and the equivalent circuit (the inset shows an expanded view of the high-frequency region of the plots).

extraction tests. Although the exact mechanism of Mn-doping in improving interface stability at elevated temperatures is a subject of further study, its possible roles include reduction of TiO_2 dissolution into the electrolyte and better retention of nanosheet morphology, which keeps a comparably high electroactive area and thus causes less performance degradation. In addition, during recharge, doped Mn ions may have also made it easier to break some covalent Li−O bonds whose presence is believed to account for a partial loss of charge capacity as reported by Hadjean et al.[50]

4. CONCLUSION

In summary, a simple and effective strategy is developed based on the hydrothermal method and ion-exchange process to obtain Mn-doped TiO_2 nanosheet-based spheres. Compared to TiO_2 nanosheet-based spheres without doping, the Mn-doped sample exhibits superior reversible capacity, improved cycling stability and rate capability when used as lithium ion battery electrodes. The improved electrochemical performance can be ascribed to the roles of Mn ions in inhibiting crystal structure conversion under calcination and improving the electrode/electrolyte interface stability. All of these effects make Mn ion-exchanged TiO_2 a promising anode for a next generation of LIBs. And the proposed synthesis strategy would also open up new opportunities in the development of high-performance nanostructures used in relevant fields.

■ ASSOCIATED CONTENT

Ⓢ Supporting Information

This material is available free of charge via the Internet at http://pubs.acs.org.

■ AUTHOR INFORMATION

Corresponding Authors

*E-mail: liud@alfred.edu.

*E-mail: xingcheng.xiao@gm.com.

Notes

The authors declare no competing financial interest.

■ REFERENCES

(1) Choi, N. S.; Chen, Z. H.; Freunberger, S. A. X.; Ji, L.; Sun, Y. K.; Yushin, K. G.; Nazar, L. F.; Cho, J.; Bruce, P. G. Challenges Facing

Lithium Batteries and Electrical Double-Layer Capacitors. *Angew. Chem., Int. Ed.* **2012**, *51*, 9994−10024.
(2) Hu, Y. S.; Guo, Y. G.; Sigle, W.; Hore, S.; Balaya, P.; Maier, J. Electrochemical Lithiation Synthesis of Nanoporous Materials with Superior Catalytic and Capacitive Activity. *Nat. Mater.* **2006**, *5*, 713.
(3) Prabaharan, S. R. S.; Michael, M. S.; Radhakrishna, S.; Julien, C. Novel Low-Temperature Synthesis and Characterization of $LiNiVO_4$ for High-Voltage Li Ion Batteries. *J. Mater. Chem.* **1997**, *7*, 1791−1796.
(4) MacNeil, D. D.; Dahn, J. R. The Reactions of $Li_{0.5}CoO_2$ with Nonaqueous Solvents at Elevated Temperatures. *J. Electrochem. Soc.* **2002**, *149*, A912−A919.
(5) Saadoune, I.; Delmas, C. $LiNi_{1-y}Co_yO_2$ Positive Electrode Materials: Relationships Between the Structure, Physical Properties and Electrochemical Behavior. *J. Mater. Chem.* **1996**, *6*, 193−199.
(6) Goodenough, J. B.; Abruña, H. D.; Buchanan, M. V. *Basic Research Needs for Electric Energy Storage: Report of the Basic Energy Sciences Workshop on Electrical Energy Storage*; U.S. Department of Energy, Office of Basic Energy Sciences: Washington, D.C., 2007.
(7) Palacín, M. R. Recent Advances in Rechargeable Battery Materials: A Chemist's Perspective. *Chem. Soc. Rev.* **2009**, *38*, 2565−2575.
(8) Bruce, P. G.; Freunberger, S. A.; Hardwick, L. J.; Tarascon, J. M. Li−O2 and Li−S Batteries with High Energy Storage. *Nat. Mater.* **2012**, *11*, 19−29.
(9) Armand, M.; Tarascon, J. M. Building Better Batteries. *Nature* **2008**, *451*, 652−657.
(10) Andersson, A. M.; Edström, K. Chemical Composition and Morphology of the Elevated Temperature SEI on Graphite. *J. Electrochem. Soc.* **2001**, *148*, A1100−A1109.
(11) Andersson, A. M.; Edström, K.; Thomas, J. O. Characterization of the Ambient and Elevated Temperature Performance of a Graphite Electrode. *J. Power Sources* **1999**, *81*, 8−12.
(12) Myung, S. T.; Takahashi, N.; Komaba, S.; Yoon, C. S.; Sun, Y. K.; Amine, K.; Yashiro, H. Nanostructured TiO_2 and Its Application in Lithium-Ion Storage. *Adv. Funct. Mater.* **2011**, *21*, 3231−3241.
(13) Han, H.; Song, T.; Bae, J. Y.; Nazar, L. F.; Kim, H.; Paik, U. Nitridated TiO_2 Hollow Nanofibers as an Anode Material for High Power Lithium Ion Batteries. *Energy Environ. Sci.* **2011**, *4*, 4532−4536.
(14) Armstrong, G.; Armstrong, A. R.; Bruce, P. G.; Reale, P.; Scrosati, B. TiO_2(B) Nanowires as an Improved Anode Material for Lithium-Ion Batteries Containing $LiFePO_4$ or $LiNi_{0.5}Mn_{1.5}O_4$ Cathodes and a Polymer Electrolyte. *Adv. Mater.* **2006**, *18*, 2597−2600.
(15) Fröschl, T.; Hörmann, U.; Kubiak, P.; Kučerovoá, G.; Pfanzelt, M.; Weiss, C. K.; Behm, R. J.; Hüsing, N.; Kaiser, U.; Landfester, K.; Wohlfahrt-Mehrens, M. High Surface Area Crystalline Titanium Dioxide: Potential and Limits in Electrochemical Energy Storage and Catalysis. *Chem. Soc. Rev.* **2012**, *41*, 5313−5360.
(16) Yang, S.; Feng, X.; Muellen, K. Sandwich-Like, Graphene-Based Titania Nanosheets with High Surface Area for Fast Lithium Storage. *Adv. Mater.* **2011**, *23*, 3575−3579.
(17) Moriguchi, I.; Hidaka, R.; Yamada, H.; Kudo, T.; Murakami, H.; Nakashima, N. A Mesoporous Nanocomposite of TiO_2 and Carbon Nanotubes as a High-Rate Li-Intercalation Electrode Material. *Adv. Mater.* **2006**, *18*, 69−73.
(18) Han, H.; Song, T.; Lee, E. K.; Devadoss, A.; Jeon, Y.; Ha, J.; Chung, Y. C.; Choi, Y. M.; Jung, Y. G.; Paik, U. Dominant Factors Governing the Rate Capability of a TiO_2 Nanotube Anode for High Power Lithium Ion Batteries. *ACS Nano* **2012**, *6*, 8308−8315.
(19) Liu, J.; Chen, J. S.; Wei, X.; Lou, X. W.; Liu, X. W. Sandwich-Like, Stacked Ultrathin Titanate Nanosheets for Ultrafast Lithium Storage. *Adv. Mater.* **2011**, *23*, 998−1002.
(20) Ye, J.; Liu, W.; Cai, J.; Chen, S.; Zhao, X.; Zhou, H.; Qi, L. Nanoporous Anatase TiO_2 Mesocrystals: Additive-Free Synthesis, Remarkable Crystalline-Phase Stability, and Improved Lithium Insertion Behavior. *J. Am. Chem. Soc.* **2011**, *133*, 933−940.
(21) Bruce, P. G.; Scrosati, B.; Tarascon, J. M. Nanomaterials for Rechargeable Lithium Batteries. *Angew. Chem., Int. Ed.* **2008**, *47*, 2930−2946.
(22) Chen, J. S.; Archer, L. A.; Lou, X. W. SnO_2 Hollow structure and TiO_2 Nanosheet for Lithium-Ion Batteries. *J. Mater. Chem.* **2011**, *21*, 9912−9924.
(23) Wu, H. B.; Chen, J. S.; Hng, H. H.; Lou, X. W. Nanostructured Metal Oxide-Based Materials as Advanced Anodes for Lithium-Ion Batteries. *Nanoscale* **2012**, *4*, 2526−2542.
(24) Wang, J.; Zhou, Y. K.; Hu, Y. Y.; Hayre, R. O.; Shao, Z. P. Facile Synthesis of Nanocrystalline TiO_2 Mesoporous Microspheres for Lithium-Ion Batteries. *J. Phys. Chem. C* **2011**, *115*, 2529−2536.
(25) Pfanzelt, M.; Kubiak, P.; Hoermann, U.; Kaiser, U.; Wohlfahrt-Mehrens, M. Preparation, Characterization, and Electrochemical Performances of Carbon-Coated TiO_2 Anatase. *Ionics* **2009**, *15*, 657−663.
(26) Mancini, M.; Kubiak, P.; Geserick, J.; Marassi, R.; Huesing, N.; Wohlfahrt-Mehrens, M. Mesoporous Anatase TiO_2 Composite Electrodes: Electrochemical Characterization and High Rate Performances. *J. Power Sources* **2009**, *189*, 585−589.
(27) Xiao, X. C.; Lu, P.; Ahn, D. Ultrathin Multifunctional Oxide Coatings for Lithium Ion Batteries. *Adv. Mater.* **2011**, *23*, 3911−3915.
(28) Chen, D. H.; Cao, L.; Huang, F. Z.; Imperia, P.; Cheng, Y. B.; Caruso, R. A. Synthesis of Monodisperse Mesoporous Titania Beads with Controllable Diameter, High Surface Areas, and Variable Pore Diameters (14−23 nm). *J. Am. Chem. Soc.* **2010**, *132*, 4438−4444.
(29) Szirmai, P.; Horváth, E.; Náfrádi, B.; Mickovic, Z.; Smajda, R.; Djokic, D. M.; Schenk, K.; Forró, L.; Magrez, A. Synthesis of Homogeneous Manganese-Doped Titanium Oxide Nanotubes from Titanate Precursors. *J. Phys. Chem. C* **2013**, *117*, 697−702.
(30) Södergren, S.; Siegbahn, H.; Rensmo, H.; Lindström, H.; Hagfeldt, A.; Lindquist, S. E. Lithium Intercalation in Nanoporous Anatase TiO_2 Studied with XPS. *J. Phys. Chem. C* **1997**, *101*, 3087−3090.
(31) Langell, M. A.; Hutchings, C. W.; Carson, G. A.; Nassir, M. H. High Resolution Electron Loss Spectroscopy of MnO(100) and Oxidized MnO(100). *J. Vac. Sci. Technol. A* **1996**, *14*, 1656−1661.
(32) Nesbitt, H. W.; Banerjee, D. Interpretation of XPS Mn(2p) Spectra of Mn Oxyhyroxides and Constraints on the Mechanism of MnO_2 precipitation. *Am. Mineral.* **1998**, *83*, 305−315.
(33) Lowell, S.; Shields, J. E.; Thomas, M. A.; Thommes, M. *Characterization of Porous Solids and Powders: Surface Area, Pore Size and Density*; Kluwer: London, 2004.
(34) Guo, J. X.; Wu, D. D.; Zhang, L.; Gong, M. C.; Zhao, M.; Chen, Y. Q. Preparation of Nanometric CeO_2-ZrO_2-Nd_2O_3 Solid Solution and Its Catalytic Performances. *J. Alloy. Compd.* **2008**, *460*, 485−490.
(35) Zhang, J. W.; Zhang, J. W.; Jin, Z. S.; Wu, Z. S.; Zhang, Z. J. Electrochemical Lithium Storage Capacity of Nickel Mono-Oxide Loaded Anatase Titanium Dioxide Nanotubes. *Ionics* **2012**, *18*, 861−866.
(36) Vázquez-Cuchillo, O.; Cruz-López, A.; Bautista-Carrillo, L. M.; Bautista-Hernández, A.; Torres Martínez, L. M.; Lee, S. W. Synthesis of TiO_2 Using Different Hydrolysis Catalysts and Doped with Zn for Efficient Degradation of Aqueous Phase Pollutants under UV Light. *Res. Chem. Intermed.* **2010**, *36*, 103−113.
(37) Xi, G.; Xiong, K.; Zhao, Q.; Zhang, R.; Zhang, H.; Qian, Y. Nucleation−Dissolution−Recrystallization: A New Growth Mechanism for *t*-Selenium Nanotubes. *Cryst. Growth Des.* **2006**, *6*, 577−582.
(38) Sutradhar, N.; Pahari, S. K.; Jayachandran, M.; Stephan, A. M.; Nair, J. R.; Subramanian, B.; Bajaj, H. C.; Mody, H. M.; Panda, A. B. Organic Free Low Temperature Direct Synthesis of Hierarchical Protonated Layered Titanates/Anatase TiO_2 Hollow Spheres and their Task-Specific Applications. *J. Mater. Chem. A* **2013**, *1*, 9122−9131.
(39) Tao, Y. G.; Xu, Y. Q.; Pan, J.; Gu, H.; Qin, C. Y.; Zhou, P. Glycine Assisted Synthesis of Flower-Like TiO_2 Hierarchical Spheres and Its Application in Photocatalysis. *Mater. Sci. Eng. B* **2012**, *177*, 1664−1671.
(40) Zhang, L. S.; Wang, W. Z.; Chen, Z. G.; Zhou, L.; Xu, H. L.; Zhu, W. Fabrication of Flower-Like Bi_2WO_6 Superstructures as High Performance Visible-Light Driven Photocatalysts. *J. Mater. Chem.* **2007**, *17*, 2526−2532.

(41) Liu, B.; Boercker, J. E.; Aydil, E. S. Oriented Single Crystalline Titanium Dioxide Nanowires. *Nanotechnology* **2008**, *19*, 505604.
(42) Pradhan, S. W.; Mao, Y.; Wong, S. S.; Chupas, P.; Petkov, V. Atomic-Scale Structure of Nanosize Titania and Titanate: Particles, Wires and Tubes. *Chem. Mater.* **2007**, *19*, 6180−6186.
(43) Ye, M. D.; Chen, C.; Lv, M. Q.; Zheng, D. J.; Guo, W. X.; Lin, C. J. Facile and Effective Synthesis of Hierarchical TiO_2 Spheres for Efficient Dye-Sensitized Solar Cells. *Nanoscale* **2013**, *5*, 6577−6583.
(44) Zhang, H.; Yang, D.; Li, D. S.; Ma, X. Y.; Li, S. Z.; Que, D. L. Controllable Growth of ZnO Microcrystals by a Capping-Molecule-Assisted Hydrothermal Process. *Cryst. Growth Des.* **2005**, *5*, 547−550.
(45) Dong, S. J.; Li, F. B. Researches on Chemically Modified Electrodes: Part XV. Preparation and Electrochromism of the Vanadium Hexacyanoferrate Film Modified Electrode. *J. Electroanal. Chem.* **1986**, *210*, 31−44.
(46) Hutching, G. S.; Lu, Q.; Jiao, F. Synthesis and Electrochemistry of Nanocrystalline M-TiO_2 (M = Mn, Fe, Co, Ni, Cu) Anatase. *J. Electrochem. Soc.* **2013**, *160*, A511−A515.
(47) Shins, J. Y.; Samuelis, D.; Maier, J. Sustained Lithium-Storage Performance of Hierarchical, Nanoporous Anatase TiO_2 at High Rates: Emphasis on Interfacial Storage Phenomena. *Adv. Funct. Mater.* **2011**, *21*, 3464−3472.
(48) Liu, D. W.; Liu, Y. Y.; Garcia, B. B.; Zhang, Q. F.; Pan, A. Q.; Jeong, Y. H.; Cao, G. Z. V_2O_5 Xerogel Electrodes with Much Enhanced Lithium-Ion Intercalation Properties with N_2 Annealing. *J. Mater. Chem.* **2009**, *19*, 8789−8795.
(49) Yu, D. M.; Zhang, S. T.; Liu, D. W.; Zhou, X. Y.; Xie, S. H.; Zhang, Q. F.; Liu, Y. Y.; Cao, G. Z. Effect of Manganese Doping on Li-ion Intercalation Properties of V_2O_5 Films. *J. Mater. Chem.* **2010**, *20*, 10841−10846.
(50) Baddour-Hadjean, R.; Pereira-Ramos, J. P. New Structural Approach of Lithium Intercalation Using Raman Spectroscopy. *J. Power Sources* **2007**, *174*, 1188−1192.